PAUL SCHERRER INSTITUT

PSI

PRACTICAL COURSE

NEUTRON GRATING INTERFEROMETRY

Magnetization response of bulk ferromagnetic domain structures visualized by neutron dark-field imaging

---

Laboratory for Neutron Scattering and Imaging
Paul Scherrer Institut
CH-5232 Villigen PSI
Switzerland

Christian Grünzweig

christian.gruenzweig@psi.ch
Tel.: 056 310 4662

Ralph Harti

ralph.harti@psi.ch
Tel.: 056 310 5086

Jacopo Valsecchi

jacopo.valsecchi@psi.ch
Tel.: 056 310 4712

Abstract

In this practical, the neutron grating interferometer (nGI) technique is used for the investigation of magnetic domain structures in Grain-oriented electrical steels (used in industrial transformer applications) at the Swiss Spallation Neutron Source (SINQ) using the cold neutron imaging facility ICON. In contrast to the attenuation based transmission image, the dark-field image (DFI) obtained in nGI is related to multiple refraction of unpolarized neutrons at magnetic domain walls. Thereby the use of the DFI allows for the volume visualization of bulk magnetic domain structures in two dimensions with a spatial resolution down to 70 µm and field of view of up to 30 mm × 30 mm. In particular, you will install the nGI setup at the beam line and you investigate the domain formation and growth along the initial magnetization curve up to the saturated state. For decreasing field, you visualize the recurrence of the hysteretic domain structure down to the remanent state.

Table of Contents

1 Motivation

Weiss postulated in 1907 that magnetic samples are subdivided into elementary domains, each having an arbitrary magnetization direction. The first observation of these domains was achieved on the surface by Bitter in 1931, with the help of a powder method. Today, a range of experimental techniques exists for the observation of surface domains like Kerr microscopy or magnetic force microscopy, and for the investigation of domains in thin film samples, provided they are transparent for electrons such as Lorentz microscopy or for X-rays such as spectro-microscopy. The investigation of internal domains in macroscopic bulk metallic materials, however, still remains a significant challenge. The exceptional case is the Libovicky method. However, this method is only applicable for alloys with a composition of Fe 12.8at%Si. Moreover this method is destructive, as the specimen has to be cut to access the internal domains. An overview of well-established domain observation techniques can be found in the text book “Magnetic Domains”.

Despite the multiplicity of domain observation techniques today, it is interesting to point out that little is known about the internal domain structure of bulk ferromagnetic materials. A large part of our understanding of magnetic microstructures in bulk materials relies on theoretical considerations, like those of phase theory in conjunction with the analysis of magnetization and magnetostriction measurements. For soft magnetic sheets or plates, such as those used in electrical machines or other inductive devices, there is a chance to image the magnetic microstructure, because these samples have large single-crystalline grains, which extend through the thickness of the sheet. Therefore many essential features of the domain structures in such materials can be studied on single crystals. For sample thicknesses larger than the domain width, materials are classified as bulk materials, even if they are only some microns thick. Neutron based techniques have the advantage that neutrons can penetrate centimeter thick samples. Therefore, these techniques have the ability to look into bulk magnetic domain structures and are not limited to the surface or thin films.

In this practical course, you will work with a novel neutron imaging approach that delivers insight into bulk magnetic domain structures. The approach relies on a neutron interferometer setup based on diffraction gratings. The relaxed requirements on spatial and temporal coherence of the grating interferometer setup lead to exposure times that are comparable to other “non-neutron” domain observation techniques. The setup is capable of working with a partially chromatic spectrum and beam sizes of several centimeters in diameter. The field of view of the setup extends up to 64 x 64 mm^2 and offers spatial resolution of about 70 µm.

The experimental results which you obtain within this practical course are based on so called dark-field images (DFI). The image contrast is based on the fact that the spatial coherence of the neutron wave front can be changed through small-angle scattering of unpolarized neutrons at, for example, magnetic domain walls. The grating interferometer technique is capable of measuring scattering angles of about 10^{-6} rad. In this practical you will learn how this technique can be used to visualize internal bulk magnetic domain structures with unprecedented quality and is well suited to investigate materials under the influence of external parameters, such as external magnetic field to visualize bulk magnetization processes.

2 Theoretical background

In the second chapter the description of the underlying and determining magnetic domain structures in grain-oriented electrical steels is given. The magnetization behavior of the domain structures is explained for externally applied magnetic fields. The theoretical description of the refraction of unpolarized neutrons at magnetic domain walls inside ferromagnetic samples is introduced.

2.1 Grain-oriented laminations and their domain structures

Grain-oriented laminations

Grain-oriented (GRO) electrical steel laminations are magnetically highly anisotropic and provide their magnetic properties in a dedicated direction only, the rolling direction. GRO-steels are solely available as a thin sheet with a thickness of less than 1 mm. Preferably, they are produced even thinner with a thickness of 350 µm down to 175 µm, with respect to their dedicated applications. The main application for GRO laminations is the manufacturing of transformer cores, power reactors and hydro-generators. They are used wherever the magnetic flux path has to be entirely or predominantly in a single direction.

GRO laminations usually have a silicon level of ≈3 %. The properties of GRO laminations are optimized in the rolling direction, which is achieved through a very dedicated production routine, including several cold and hot rolling, annealing, pickling and hardening steps. The Goss-orientation (GO), after its inventor Norman P. Goss, is the only industrial-state grain orientation. Others, such as cube orientation, have not been produced on an industrial scale. The Goss-orientation (Goss-texture) is schematically shown in Figure 1. In the Goss-orientation, the crystal orientation relative to the sheet is the [001]-direction parallel to the rolling direction, which is generally the length of the lamination. The plane parallel to the surface is the (110) crystal plane.

The crystallographic grains in GRO laminations grow very large through the various production stages for the development of the texture, giving diameters of up to several centimeters in length. These grains can be made visible by different reflections of visible light after chemical etching a GRO lamination. This is show in Figure 2. On the top, an optical photograph of a coated (glassy magnesium silicate layer) lamination is shown, where no features are visible and the lamination looks homogeneous. The bottom image shows a lamination that was uncoated before taking the photograph and reveals the large elongated grains. The texture of a steel lamination is a measure of the distribution of crystallographic orientations. Such GRO laminations are commonly characterized by the pronunciation of the Goss-texture, also called the sharpness of the texture. This sharpness can be increased up to an orientation deviation of less than 3°.

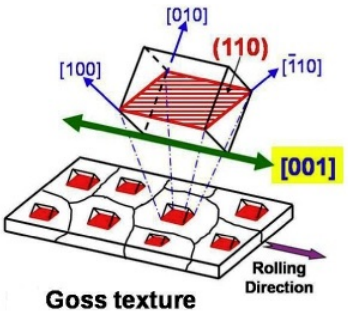

Figure 1: Goss-orientation in a steel alloy with the [001] direction parallel to the rolling direction and (110) parallel to the surface for all grains. The crystallographic cubic structure of the steel is shown as a zoom to the atomic scale on top.

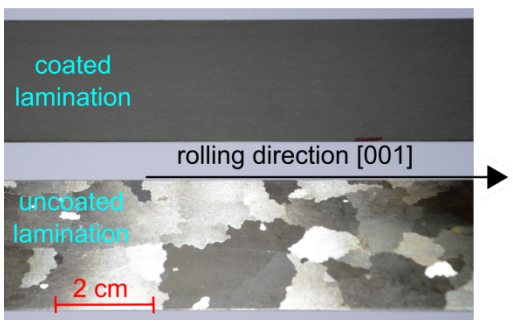

Figure 2: Optical photographs of a coated grain-oriented lamination on the top. A second optical photograph of the same lamination where the coating was chemically removed is shown in the bottom. Large grains are visible.

Basic domains:
The basic or volume magnetic domain structures of GRO laminations are slab-like volume domains that are magnetized in 180° parallel or antiparallel to the magnetic easy axis, which is the [001]-axis. A special feature in GRO lamination (also in other positive anisotropy cubic materials) are the domain walls, which are oriented in the (100) or the (010) plane, forming a "zigzag-shape", as visible in the schematic in Figure 3(a). Given the energy of a domain wall is proportional to the length of the wall, one would expect the shortest possible domain wall to be realized, which is perpendicular to the surface (110). However in GRO laminations the energy for a domain wall in the (100) and (010) plane is the lowest. The balance of these two energy reductions lead to the shortest domain walls (110) tending to rotate towards the above mentioned orientation and "zigzag-shape". In Figure 3(a) the basic domains with the magnetization, marked by arrows, pointing along and opposed to the [001] direction and the gray domain walls, oriented along the [010] and [100] direction, are shown. The SEM image in Figure 3(b) shows the surface magnetic domain structure in such a GRO lamination in the top view. These domains form the basis for the magnetic flux transport in the sample hence they are called basic domains.

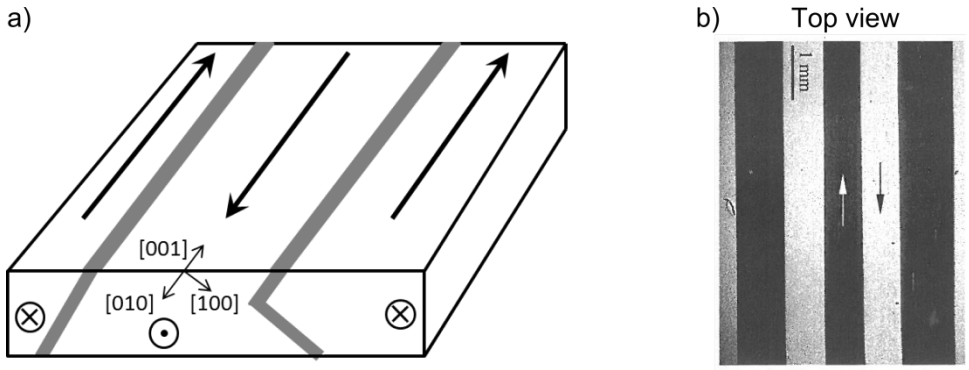

Figure 3: Basic domain structure in Goss-oriented samples: a) Schematic of basic magnetic domains and their domain walls in a GRO lamination. Magnetization pointing in rolling direction ([001]) and domain walls along the preferred orientation along the [010]- and [100]-axis. b) Electron backscattering image of an ideally oriented grain in an GRO lamination, showing wide volume domains (up to several mm in width) with magnetization pointing in ± [001]- direction.

Supplementary domains:
Perfectly oriented grains, with a magnetic easy axis in the surface, display only simple magnetic domain pattern. The patterns get much more complex in slightly misoriented grains. The misorientation of a grain is characterized by the angle between the surface and the nearest magnetic easy axis ϑ_s which is delineated in Figure 4(a),(b) as the angle between the easy axis and a line parallel to the surface. Two different domain patterns that exist in misoriented grains in GRO laminations are schematically shown in Figure 4. In (a), standard lancet domains are present, while b) depicts a quasi-fir-tree pattern of domains. In (a), the magnetic flux is transported to the opposing surface or the neighboring domain by internal supplementary transverse domains. In (b), the flux is transported parallel to the surface to the next domain. The underlying principle of both patterns is the introduction of small supplementary surface domains, which collect the flux. Without these supplementary domains the magnetic flux would escape from the surface leading to energetically unfavorable magnetic stray fields. Thus the effective size of domains at the surface is decreased and the flux that needs to be diverted is distributed onto these supplementary domains. Due to the fact that these compensating domains are superimposed on the basic domain structure, these domains are called supplementary domains.

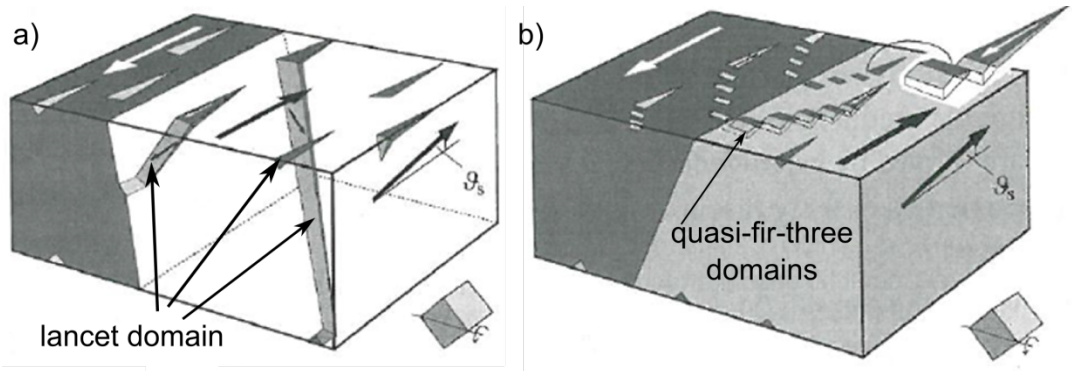

Figure 4: Two possible supplementary domain patterns in a GRO lamination. a) Sketch of two basic domains with supplementary lancet domains as they can be observed in a misoriented (110) crystal. The flux is transported to the opposite surface by internal transverse domains. b) Two basic domains with an alternative quasi-fir-tree pattern. The flux is transported to the adjoining domains, parallel to the surface.

2.2 Behavior of domain walls during magnetization

The underlying internal structure of magnetic domains and domain walls in GRO laminations is essential for their magnetic behavior and performance. Without easily displaceable domain walls, providing the necessary permeability, modern electrical machines would simply not work.
Two processes are responsible for the magnetization of a GRO lamination on the domain level. Either the domain walls start to move or the magnetization of the domains is rotated in response to an applied magnetic field.
The domain wall movement magnetization behavior holds for samples, where the domains' magnetization is pointing only in the direction of the applied field or opposite, like the basic domain structure in a GRO lamination. Applying a magnetic field causes the domain walls to move so as to increase the size of domains whose magnetization is lying parallel to the applied field, at the cost of the sizes of domains whose magnetization is opposing the field. This behavior can be explained by the Zeeman energy E_{Ze} , which is the energy arising from the interaction of a magnetic domain with an externally applied magnetic field :

$$E_{Ze} = -\mu_0 \int_V \vec{M} \cdot \vec{H_{ext}} dV \qquad \text{(Eqn. 1)}$$

Therefore, the Zeeman energy is proportional to the negative of the cosine of the angle β (seen in Fig. 5) between magnetization of the domain *M* and the externally applied field H_{ext}. In Figure 5 are the domains with their magnetization oriented parallel to the applied field reduce this energy, while domains with their magnetic field oriented opposite to the applied field increase the Zeeman energy. This process is schematically visualized in Figure 5 (a). The top part of the image shows a sample with two antiparallel magnetized domains without an external field. In the bottom part of Figure 5(a), the externally applied magnetic field H leads to a growth of the domain parallel to H (β= 0°) on the cost of the domain which is magnetized in the opposite direction (β = 180°). If magnetic domains are perpendicular to the applied external field, the magnetization *M* of the domains will rotate. This is schematically shown in Figure 5(b). The upper scheme shows the domain state for two antiparallel magnetized domains without an external field. On this occasion, the field is applied in perpendicular direction (β = 90°/-90°). In the bottom sketch, the magnetization of both domains is rotated by 45° due to the applied field. The rotation angle depends on the strength of the applied field *H*. If domains with magnetization directions between parallel and perpendicular are present, like in supplementary domain structures, both, the domain wall motion and the magnetization rotation, play a role.

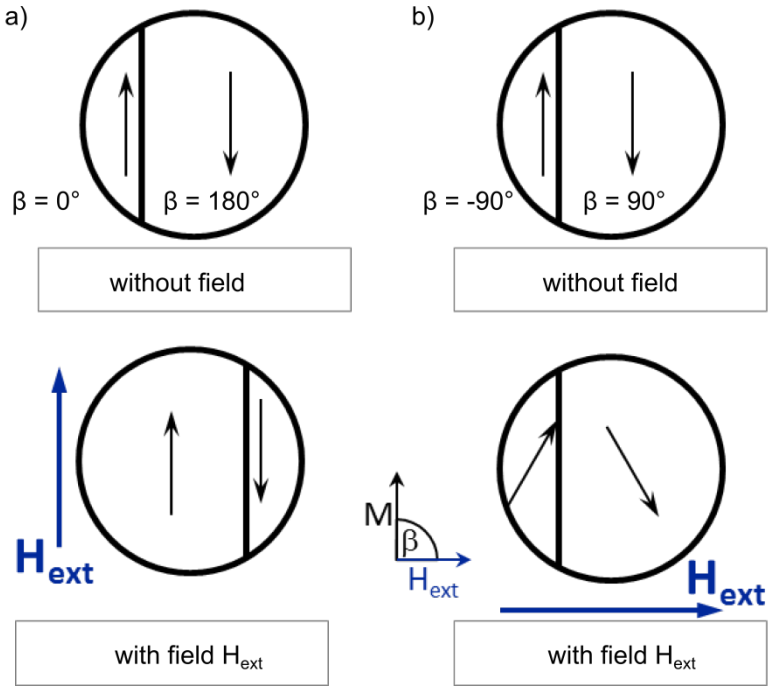

Figure 5: Two different processes of magnetization: a) Schematical of magnetization by domain wall motion is shown. Domains with magnetization M parallel (β = 0°) or antiparallel (β =180°) to the applied field H grow or shrink by domain wall motion. b) Magnetization by domain rotation is schematically illustrated for domains with magnetization M perpendicular (β = ±90°) to the applied field H_{ext}.

Starting to magnetize a realistic sample, both processes happen at the same time and cannot be sharply distinguished. Although a rough separation is shown in Figure 6 and can be described as follows: Domain wall motion is the main process up to about the "knee" of the magnetization curve B_k ; from there to saturation magnetization M_s , rotation predominates. In the region above the knee, work must be done against the anisotropy forces (magnetization is rotated out of the magnetic easy direction) and a large increase in the applied field *H* is required for relatively small increases in the magnetization *M*.

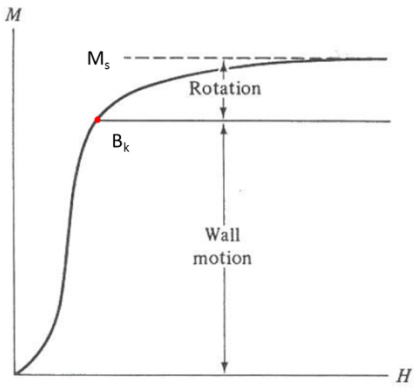

Figure 6: General separation of the magnetization process into the process of domain wall motion and magnetization rotation. The saturation magnetization M_S and the knee of the magnetization curve B_k are marked.

2.3 Refraction of neutrons at magnetic domain walls

The spontaneous magnetization in ferromagnetic samples occurs from the magnetic moments of adjacent atoms being parallel. Regions of atoms with magnetic moments pointing in the equal direction are called magnetic domain. Each magnetic domain is described by the magnetic induction *B*, as can be seen in Figure 7. Inside each domain, the magnetization points along a magnetic easy axis with the value of the saturation magnetization B_s. For a cubic crystal like FeSi the directions *x*,*y* and *z* delineated in Fig. 7 correspond to the crystallographic (001),(010) and (100) directions, respectively.

The transition region between the two domains, called the domain wall, is the area, where the magnetization rotates out of the easy direction. For Bloch domain walls, mostly present in GRO laminations, the magnetization rotates through the plane of the wall, while for Neél walls the magnetization rotates in the plane of the wall. The thickness of the domain wall depends on the anisotropy of the material and is in the range of some nm for iron. Additionally a neutron beam is schematically included in Figure 7, which points onto the domain wall.

Neutrons are able to interact with the atomic nucleus and the magnetic moments of the atomic shells with their magnetic moment μ_N. The refraction of neutrons in magnetic materials can only be described correctly using dynamical approaches. Therefore, the Schrödinger equation with a spin-dependent potential, depending on the average homogeneous magnetic induction, needs to be taken for the description of the neutrons refraction. To do so, the domain walls are assumed to be infinitely thin and as a plane plate. This assumption is allowed as the neutrons velocity being too large for an interaction with the magnetic moments of the atoms in the wall while passing through. It is called a non-adiabatic penetration process. Hence it is not necessary to investigate the neutrons behavior inside the domain wall. This is in analogy to the Snell's law in optics, which describes the refraction of a light beam at an interface of changing refractive indices by simply the two refractive indices.

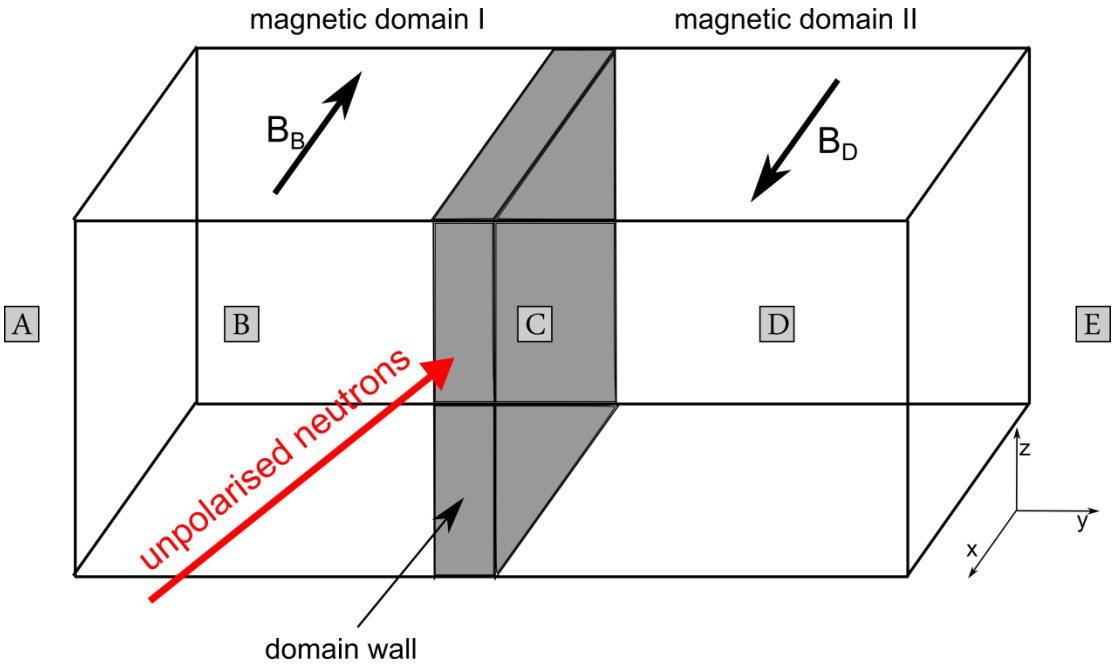

Figure 7: Schematic of a plane domain wall separating two neighboring magnetic domains with different magnetic inductions B. The neutrons transverse in series the regions A,B,C,D and E. Region A: Free space (air) outside the sample. Here no magnetic induction is present (B = 0). Region B: Magnetic domain I with constant magnetic induction BB. Region C: The domain wall with rotating magnetic induction. Region D: Magnetic domain II with constant magnetic induction BD. Region E: Free space (air) outside the sample (B = 0).

To calculate the refraction angles, we consider the refraction of unpolarized neutrons at domain walls as a boundary value problem of the Schrödinger equation including a spin dependent potential. Consequently, the Hamilton operator *H* is then given by:

$$H = -\frac{\hbar^2}{2m}\nabla^2 + V_{nuc}(\mathbf{r}) - \mu_N \cdot \mathbf{B}(\mathbf{r}) \qquad \text{(Eqn.2)}$$

using the mass of the neutron *m*, the nuclear interaction potential $V_{nuc}(\boldsymbol{r})$ and the product of μ_N and $\boldsymbol{B(r)}$ for the magnetic interaction potential. Passing through one magnetic domain, the neutron experiences only a constant interaction potential, allowing for the calculation of its behavior with the time-independent Schrödinger equation inside one domain

$$H\psi(\mathbf{r}) = E\psi(\mathbf{r}). \qquad \text{(Eqn. 3)}$$

Here $\psi(\boldsymbol{r}) = \begin{pmatrix}\psi\uparrow\\ \psi\downarrow\end{pmatrix}$ is the spinor of the neutrons. The total energy of a free neutron can be given as $E = \frac{\hbar^2 k^2}{2m}$ and the wave equation of a neutron in a magnetic material turns out to be:

$$(\nabla^2 + k^2)\psi(\mathbf{r}) - \frac{2m}{\hbar^2}\left[V_{nuc}(\mathbf{r}) + \mu_N \cdot \sigma \cdot \mathbf{B}(r)\right]\psi(\mathbf{r}) = 0. \qquad \text{(Eqn. 4)}$$

Here, σ= (σ_x, σ_y, σ_z) is composed of the 2x2 Pauli spin matrices. This is the vector that couples all components of the spin to the magnetic induction ***B***. When entering a region of homogeneous magnetization, a neutron experiences a potential jump, which is depending on the spin state of the neutron (parallel or antiparallel to the magnetic induction ***B***). The steadiness of the wave function and its derivatives at the magnetic sample surface is the boundary condition. Note, that inside the sample a constant nuclear potential is assumed, thereby only the magnetic potential jump needs to be taken into account, when calculating the neutrons behavior while traversing a magnetic domain wall.

Due to the domain wall being considered infinitely thin, the neutron passes non-adiabatically through the wall, resulting in the neutrons spin being not able to follow the rotation of the magnetic induction in the wall, and therefore the spin is fixed during the passage. The Larmor frequency of the neutron is given by $\omega_L = \frac{2|\mu_N|\cdot|\boldsymbol{B}_S|}{\hbar}$. The probability of refraction for the neutron passing the domain wall, where the magnetic induction rotates with a frequency ω is determined by the ratio $\frac{\omega}{\omega_L}$. As a consequence, behind a domain wall three different neutron beams exist. An unrefracted, unpolarised beam and two refracted spin-polarized beams, which are displaced by a certain angle compared to the incident beam. In analogy to the nuclear potential, the magnetic potential is also assumed to have an averaged magnetic induction $\boldsymbol{B}_{AV} = \mu_0\boldsymbol{H}_{AV} + \boldsymbol{M}_{AV}$ and furthermore the sample is considered as a continuum instead of a lattice.

The Schrödinger equation (Eqn. 4) is solved by a spinor of the form

$$\psi(\mathbf{r}) = c \cdot e^{i\mathbf{k}_{p,a}\cdot\mathbf{r}} \qquad \text{(Eqn. 5)}$$

while $\boldsymbol{k}_{p,a}$ are the wave vectors for the neutron with spin parallel or antiparallel to $\boldsymbol{B}_{AV}$:

$$\mathbf{k}_p^2 = k^2 - \Delta k^2 - k_{B_{AV}}^2 \quad \text{and} \quad \mathbf{k}_a^2 = k^2 - \Delta k^2 + k_{B_{AV}}^2. \qquad \text{(Eqn. 6)}$$

In this equation $\Delta k^2 = 2\pi N b_c$ accounts for the nuclear interaction potential with *N* as the scattering nuclei per unit volume and b_c as the coherent scattering length. $k_{B_{AV}}^2 = \frac{2m}{\hbar^2}\mu_N|\boldsymbol{B}_{AV}|$ for the magnetic interaction. The spatially dependent refractive index $n(\boldsymbol{r})$ for neutrons is defined as the ratio of the wave vector inside a medium $\boldsymbol{K(r)}$ and the free space wave vector $\boldsymbol{k}$

$$n(\mathbf{r}) = \frac{\mathbf{K}(\mathbf{r})}{\mathbf{k}} = \sqrt{1 - \frac{V(\mathbf{r})}{E}} \qquad \text{(Eqn. 7)}$$

Substituting the wave vectors in Eqn. 7 results in an additional spin dependent potential contribution for magnetic materials:

$$n^2 = \frac{k_{p,a}^2}{k^2} = \frac{k^2 - \Delta k^2 \pm k_{B_{AV}}^2}{k^2} = 1 - \frac{\Delta k^2 \pm k_{B_{AV}}^2}{k^2}. \qquad \text{(Eqn. 8)}$$

As visible in Figure 7, ferromagnetic samples behave as birefringent materials for a beam of unpolarised neutrons, due to the refractive indices inside the sample being related to the magnetic induction ***B***. When neutrons penetrate a ferromagnetic sample, the first refraction occurs at the sample surface, where the first transition from air A into the first magnetic domain B occurs (compare Figure 7). A second refraction takes place at the domain wall. Due to the assumption of a homogeneous material in respect to the nuclear interaction potential the refractive index is given by just the magnetic potential changes

$$n^2 = \frac{k^2 \pm k_{B_{AV}}^2}{k^2 \mp k_{B_{AV}}^2}. \qquad \text{(Eqn. 9)}$$

The whole process of the refraction of an unpolarised neutron beam at a sample surface and a magnetic domain wall is illustrated in Figure 8. Here, a domain wall separates two magnetic domains with opposite magnetic induction (compare also Figure 7).

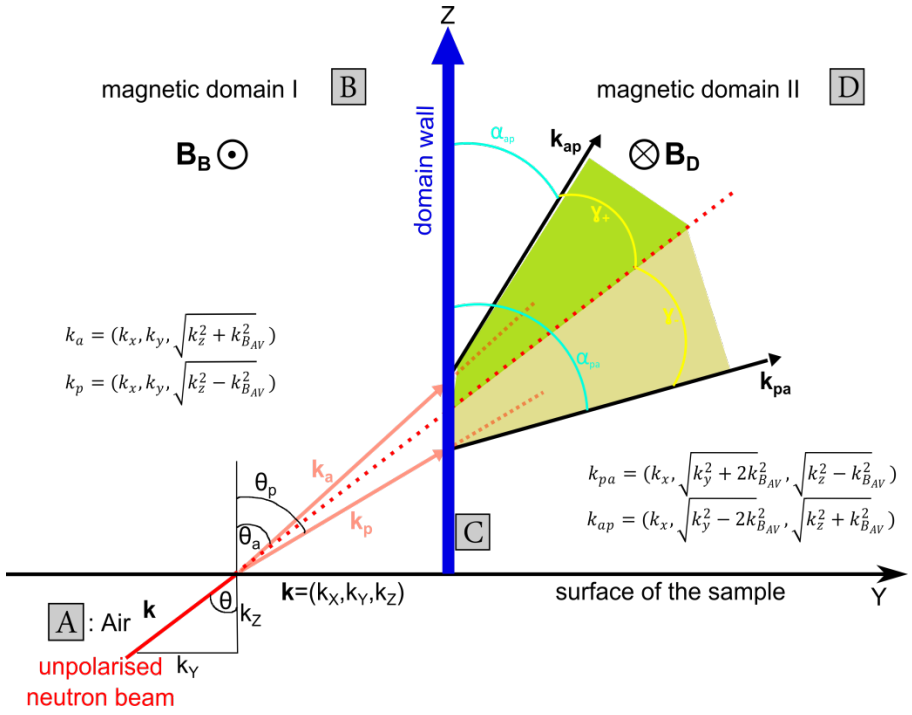

Figure 8: Mechanism of the refraction of an unpolarised neutron beam in a ferromagnetic sample. A domain wall separates two magnetic domains with opposite magnetic induction (compare also Figure 7). Φ and k are the angle and wave vector of incident neutron beam. The beam gets refracted at the surface of the sample and later at the magnetic domain wall. Due to the first refraction, the normal component of the wave vector k_Z jumps to $\boldsymbol{k_{Z,(p,a)}} = \sqrt{\boldsymbol{k_{Z^2}} \pm \boldsymbol{k_{B_{AV}}}^2}$. The refraction angles for spin parallel and antiparallel are named Φ_p and Φ_a. Refracted at the domain wall, the normal component k_Y changes into $\boldsymbol{k_{Y,(pa,ap)}} = \sqrt{\boldsymbol{k_{Y^2}} \pm \boldsymbol{2k_{B_{AV}}}^2}$ in dependence from the spin orientation. After being refracted at the domain wall, the refraction α_{ap} and α_{pa} can be found. The total refraction angle in the end is included as the two angles γ_+ and γ_-. No variation in the nuclear potential was included here.

Φ and $\mathbf{k} = (k_X, k_Y, k_Z)$ are the angle and wave vector of incident neutron beam. While the normal vector of the sample surface points in the z-direction, the normal vector of the domain wall points into the y-direction. The spin of the incoming neutron can either be parallel or antiparallel (marked by the index *p* and *a*) with respect to the z-direction. Due to its assumed homogeneity, the nuclear potential is neglected in the following:

$$k_{p,a}{}^2 = k^2 - \Delta k^2 \pm k_{B_{AV}}{}^2 \approx k^2 \pm k_{B_{AV}}{}^2. \qquad \text{(Eqn. 10)}$$

Thus, the beam gets refracted at the surface of the sample, where the normal component of the wave vector k_Z jumps to $k_{Z,(p,a)} = \sqrt{k_{Z^2} \pm k_{B_{AV}}{}^2}$. This results in a refraction angle at the sample surface for parallel or antiparallel spin with respect to the magnetic induction B_B of

$$\sin\theta_p = \frac{k_Y}{\sqrt{k^2 - k_{B_{AV}}{}^2}} \quad \text{or} \quad \sin\theta_a = \frac{k_Y}{\sqrt{k^2 + k_{B_{AV}}{}^2}}. \qquad \text{(Eqn. 11)}$$

At the domain wall, where the magnetic induction changes suddenly (infinitely thin domain wall), a potential jump of $\pm 2\mu_N \cdot \boldsymbol{B}_S$ with $\boldsymbol{B}_S = |\boldsymbol{B}_{AV}|$ occurs dependent on the spin configuration. As a consequence, the neutron beam gets refracted at the domain wall. The normal component k_Y changes from $-k_{BAV}{}^2$ into $+-k_{BAV}{}^2$. This is a total change of $2k_{BAV}{}^2$. Therefore, k_Y becomes $\boldsymbol{k}_{\boldsymbol{Y},(\boldsymbol{pa},\boldsymbol{ap})} = \sqrt{\boldsymbol{k}_{\boldsymbol{Y}^2} \pm 2\boldsymbol{k}_{\boldsymbol{B_{AV}}}{}^2}$ depending on the spin directions. The other components of the wave vector stay untouched. Accordingly, after being refracted at the domain wall, the refraction angles α_{pa} and α_{ap} are found as

$$\sin\alpha_{pa} = \frac{\sqrt{k_y{}^2 + 2k_{B_{AV}}}}{k^2 + k_{B_{AV}}} \qquad \text{(Eqn. 12)}$$

for spin parallel and for spin antiparallel as

$$\sin\alpha_{pa} = \frac{\sqrt{k_y{}^2 - 2k_{B_{AV}}}}{k^2 - k_{B_{AV}}}. \qquad \text{(Eqn. 13)}$$

The total refraction angles in the end γ_+ and γ_- (yellow marked in Figure 8) can be given for parallel and antiparallel by

$$\gamma_- = \alpha_{pa} - \theta = \arcsin\left(\frac{\sqrt{k_y{}^2 - 2k_{B_{AV}}}}{k^2 - k_{B_{AV}}}\right) - \theta \qquad \text{(Eqn. 14)}$$

and

$$\gamma_+ = \theta - \alpha_{ap} = \theta - \arcsin\left(\frac{\sqrt{k_y{}^2 + 2k_{B_{AV}}}}{k^2 + k_{B_{AV}}}\right). \qquad \text{(Eqn. 15)}$$

From these two equations (Equation 14 and 15) it can be seen, that the angles of refraction stay the same, independent from how the components of the wave vector $\boldsymbol{k}$ are distributed on k_X and k_Z . The angles are only depending on k_Y and k and the component of the spin in z-direction.

3 Principle of neutron grating interferometry

The principle of grating-based neutron interferometry is explained in this chapter. The interferometer setup is used in combination with a phase stepping approach to record the dark-field image. The data acquisition and processing are described in detailed which you will later use to evaluate the data.

3.1 Setup and sample environment

Grating interferometer setup

The neutron grating interferometer setup is made of three micro-structured gratings that are placed in a classical neutron imaging beam line. A schematic of the neutron grating interferometer is shown in Fig. 9. The absorbing source grating G_0 (periodicity p_0= 1076 µm, made of Gadlinium) is placed in a monochromatic neutron beam with a wavelength of 4.1 Å ($\Delta\lambda/\lambda \approx 15\%$) provided by a velocity selector. The grating G_0 can be interpreted as an array of periodic line sources providing sufficiently high spatial coherence when illuminated with a large, centimeter-sized neutron beam. The second grating G_1 (p_1= 7.97 µm, made of silicon), placed at a distance of l= 5.23 m, is used as a periodic phase modulator for the incoming neutrons. Because of the Talbot effect, the phase modulation is transferred into an intensity oscillation behind G_1 at a distance d_T. This intensity pattern is then analyzed by the third grating G_2 (p_2= 4 µm, made of Gadolinum). The grating set is shown in Fig. 10. The grating interferometry setup is combined with a state-of-the-art neutron imaging detection system. The images are recorded using a ^{6}LiF/ZnS scintillator screen and a digital camera. The effective spatial resolution of 70 µm is the result of intrinsic blurring of the scintillation screen, the optical system, and penumbra blurring caused by the sample to detector distance.

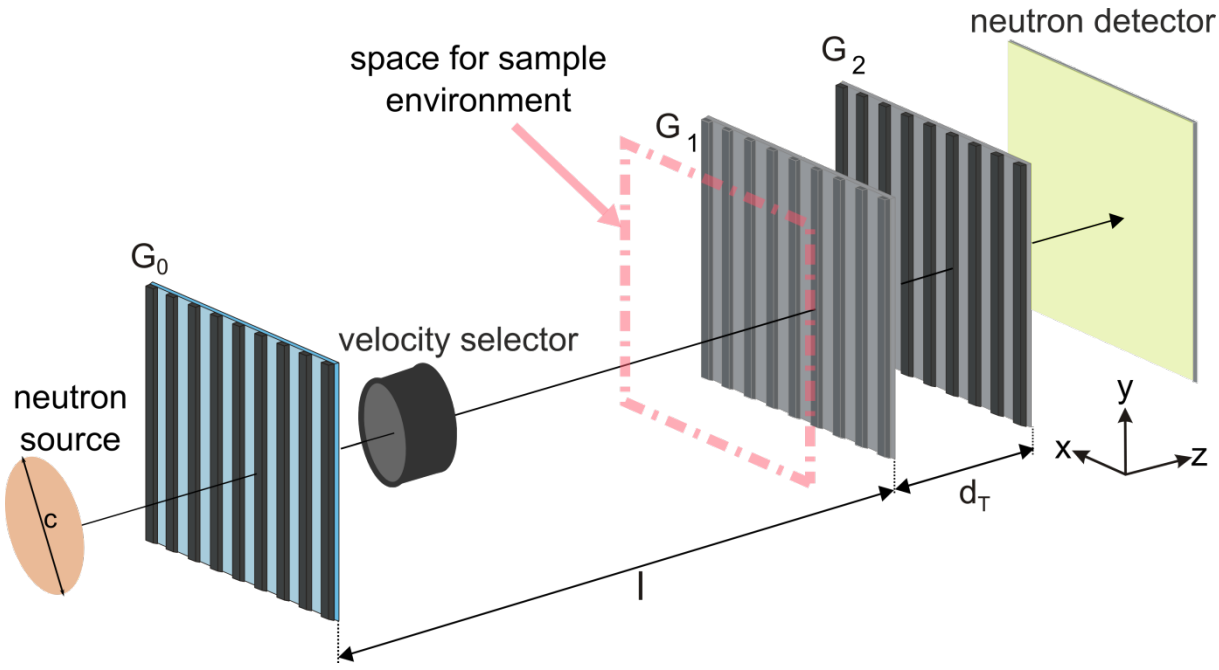

Figure 9: Schematic layout of the neutron grating interferometer including the three gratings G0, G1 and G2, a velocity selector and a conventional scintillator based neutron detection system. The distance l, the Talbot distance d_T and the source width c are included too. The magnetization frame is mounted as close as possible in front of G_1.

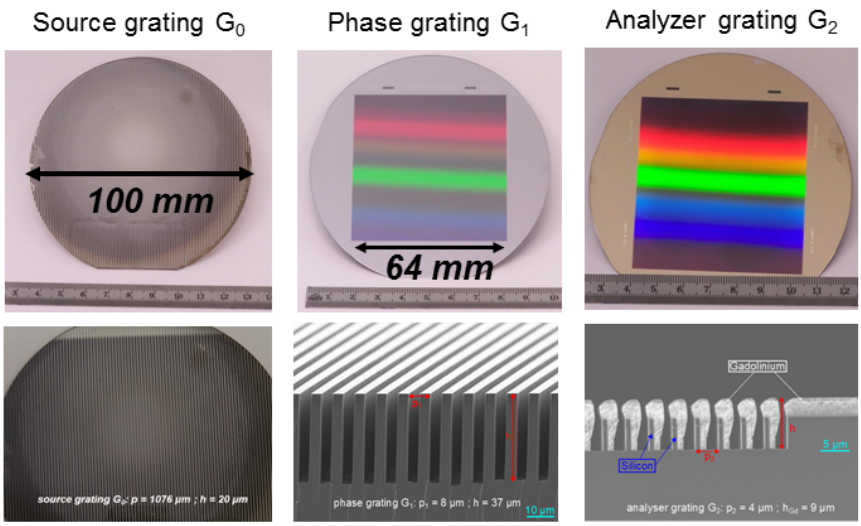

Figure 10: Optical photographs and scanning electron microscopy images of the grating set needed for a grating interferometer setup.

Magnetic sample environment

For the investigation of GRO laminations under the influence of magnetic fields a specialized sample environment is used as shown in Figure 11.

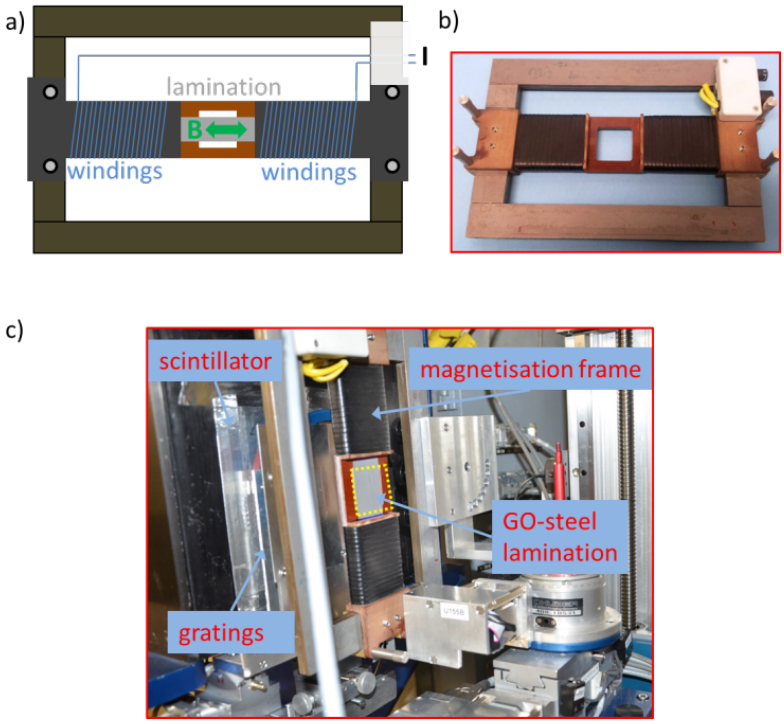

Figure 11: Magnetic sample environment. a) Simplified drawing of the frame. Supplied by a current I, the windings induce a magnetic field B (green) in the sample (gray). b) Optical photograph of the frame without sample. c) The frame as mounted in front of the gratings and the scintillator. A GRO lamination is mounted inside the windings.

In a) a simplified drawing of the frame can be seen. By a current we apply to the windings, a magnetic field *B* can be induced in the lamination. Hereby the lamination can be magnetized by DC- or AC-magnetic fields, depending on the applied current. An optical photograph of the frame is shown in b). Finally, c) shows the frame as it is placed directly in front of the grating setup (compare dashed square in Figure 9). The field of view in this experimental layout is 35 x 35 mm, limited by the magnetic frames window and indicated by the dashed, yellow box. The windings are supplied with a current up to 4 A by a power supply (KEPCO BOP100-4ML), while the power supply itself is triggered by a frequency generator (Rigol DG4000). This generator is interfaced into the control software, allowing for the automated application of magnetic fields and measuring processes. The magnetic environment used in this way is able to apply theoretically currents of up to ± 4 A in DC mode. The sample is inserted into the frame such that the coils are wound around the sample as part of the frame.
A schematic of how the magnetic sample environment is connected and installed at the beam line can be seen in Figure 12. The output-voltage signal from the frequency generator is transferred from the measuring cabin to the power supply, which is located inside the bunker, via a BNC cable. The input of a voltage of 100 mV into the power supply results in an output of 50 mA. The magnetic field produced by the frame, when supplied with 50 mA (banana jack cable), was in our case 75 A/m. Consequently the conversion factor from applied voltage to observed magnetic field was found to be $750\ \frac{A}{m \cdot V}$.

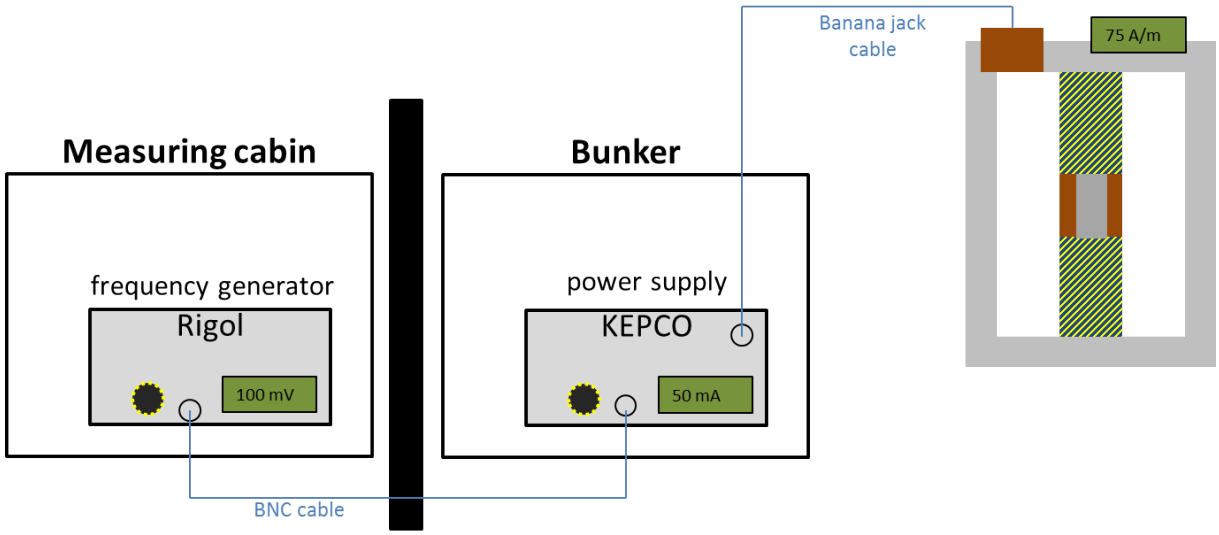

Figure 12: Frequency generator in the measuring cabin sending a voltage to the power supply in the bunker. The coils supplied with current induced a magnetic field in the sample. The conversion factor from applied voltage to observed magnetic field is 750 (A/m)·V.

3.2 Data acquisition and image processing

As shown in Figure 9 and explained at the beginning of section 3.1, an interference pattern is created behind G_1 with a period of 4 µm, due to the interplay of the first gratings G_0 and G_1. This interference pattern cannot be resolved by the imaging detector due to its small periodicity. In order to circumvent this problem, the analyzer grating G_2 is placed in the plane of the interference pattern. A spatial phase stepping approach is used, to transfer the interference pattern into an intensity modulation on the detector that is placed behind G_2 (compare also Figure 9). Scanning the analyzer grating in equidistant steps in the direction of x_{st} over one grating period p_2 results in a stack of images with different grating positions, and hence a different intensity modulation in each detector pixel is recorded. To be able to produce a dark-field image (DFI), three different sets of images need

to be recorded. Those are a stepping scan with the sample in the neutron beam (data), a stepping scan without sample inside the neutron beam (open beam) and a stack where images are taken with closed shutters (dark current). The dark current stack is used, to correct for extraneous noise in the CCD camera, which is an electronic offset. The open beam stack (same steps as performed for the collection of the data stack) is required for the correction of inhomogeneous illumination by neutrons, inhomogeneous camera sensitivity and effects such as wave front distortions originating from the gratings themselves. Note that the same principle applies regardless of which grating is stepped. We stepped the source grating G_0, which requires the lowest precision in each mechanical step due its comparably large periodicity.

The first data processing step is the background correction of all acquired data and open beam images. This is achieved by subtracting an average dark current image, formed by averaging all dark currents into one, from each single data and open beam image. Due to the phase stepping over one period, the intensity $I(m,n,x_{st})$ in each detector pixel (m,n) oscillates as a function of the stepping x_{st}. This is shown schematically in Figure 13.

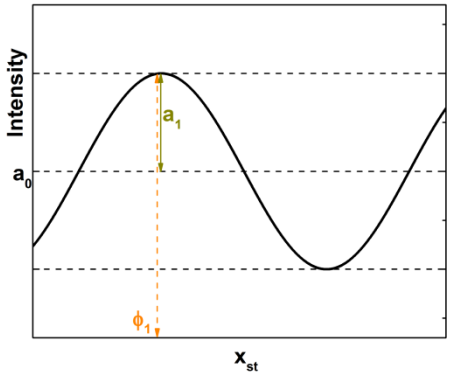

Figure 13: Schematic intensity oscillation in one detector pixel described by the amplitude a_1, the offset a_0 and the phase coefficient Φ_1 if one grating is scanned along the direction x_{st} over one grating period.

These intensity oscillations $I(m,n,x_{st})$ can be described by a Fourier series for each single detector pixel:

$$I(m,n,x_{st}) = \sum_i a_i(m,n) \cdot cos(i k x_{st} + \phi_i(m,n)) \approx a_0(m,n) + a_1(m,n) cos(k x_{st} + \phi_1(m,n)) \quad \text{(Eqn. 16)}$$

with a_i being the amplitude, Φ_i the phase and $k = 2\pi/p_2$, using the period $p2$ of G_2. A sinusoidal oscillation can be characterised by the amplitude a_1, the offset a_0 and the phase Φ_1. We can extract from the oscillation the coefficients (a_0, a_1, Φ_1) for each detector pixel (m,n). When we denote the coefficient for a pixel of an image with sample by an s and without sample by ob, we end up with the conventional transmission image (TI) of our sample by normalizing the sample image to the open beam image pixel wise:

$$\mathrm{TI}(m,n) = \frac{a_0^s(m,n)}{a_0^{ob}(m,n)}. \quad \text{(Eqn. 17)}$$

The TI, calculated that way, is analogue to the transmission image obtained in classical neutron imaging without a grating interferometer installed. The dark-field image (DFI) is formed by the analysis of the amplitude coefficients of the sample $a^s{}_1(m,n)$ and the open beam $a^{ob}{}_1(m,n)$ in each pixel. As a first step one normalizes the amplitude coefficient $a^{ob}{}_1$ to the offset $a^{ob}{}_0$ of the open beam. This results in the so-called visibility V^{ob}. This visibility determines the maximum contrast that can be produced by the interferometer

$$V(m,n) = \frac{\mathrm{I}^{ob}_{max} - \mathrm{I}^{ob}_{min}}{\mathrm{I}^{ob}_{max} + \mathrm{I}^{ob}_{min}} = \frac{\mathrm{a}^{ob}_{1}(m,n)}{\mathrm{a}^{ob}_{0}(m,n)}. \qquad \text{(Eqn. 18)}$$

For the DFI observation the normalized amplitude coefficient V^S is normalized to the visibility V^{ob} of the open beam

$$\mathrm{DFI}(m,n) = \frac{\mathrm{V}^{s}(m,n)}{\mathrm{V}^{ob}(m,n)} = \frac{\mathrm{a}^{s}_{1}(m,n)\cdot\mathrm{a}^{ob}_{0}(m,n)}{\mathrm{a}^{s}_{0}(m,n)\cdot\mathrm{a}^{ob}_{1}(m,n)}. \qquad \text{(Eqn. 19)}$$

In general the reduction of the DFI signal is proportional to the degradation of the ability of the incoming neutron beam to interfere, due to scattering or multiple refractions at potential fluctuations inside the sample

3.3 Dark-field imaging of magnetic domain structures

As derived in section 2.3, also potential fluctuations of magnetic origin can interact with neutrons and neutrons can be refracted by magnetic domain walls. Multiple refractions at domain walls will act in the same manner onto the interference pattern. Accordingly, a neutron beam undergoing multiple refractions at domain walls has a locally degraded coherence when exiting the sample. This decreases the ability of the neutrons to interfere behind the phase grating G1 and results in a local decrease of the interference pattern. This is illustrated in Figure 14, where orange lines in the sample represent magnetic domain walls. Neutrons penetrating the sample are multiply refracted and decrease the coherence of the exiting neutron beam behind the sample. This results in a degraded visibility of the interference pattern and consequently in a decreased value of the DFI. Thus the value in the DFI is correlated to the relative density of magnetic domain walls in the sample.

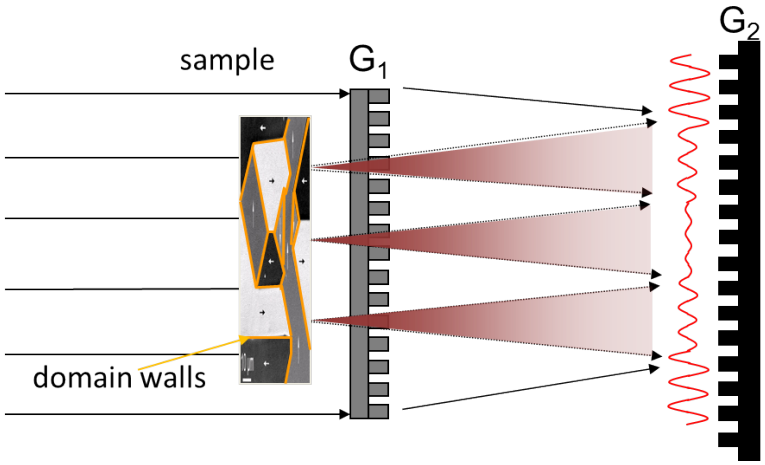

Figure 14: Multiple neutron refractions at domain walls (orange) inside a sample lead to a local degradation of the coherence and consequently to a decreased visibility of the interference pattern.

A demonstration of the visualization of a magnetic domain wall density is shown in Figure 15. In a) a schematic of the domain wall structure (red) in a magnetized and a non-magnetized steel foil is shown. The upper foil is magnetized by neodymium magnets, while the lower foil is not. The foils are both mounted on an aluminum holder. In b) the TI of the two 20 µm thick steel foils is shown. The upper foil is between the magnets the lower one does not have magnets. Both foils are invisible in the TI due to the small attenuation of steel. Only the aluminum holder and the neodymium magnets

are visible. The DFI of the two steel foils is shown in c). Here, the lower foil provides a contrast while the upper foil, between the magnets, stays invisible. This can be explained by the lower steel foil providing a high density of magnetic domains and thereby domain walls inside the foil (compare a)). These domain walls degrade the coherence of the neutron beam and thereby decrease the DFI signal.
The upper steel foil is magnetized by the attached magnets. That means the foil is in a "one-domain-state", with no domain walls inside the sample (compare schematic in a)). This results in no magnetic scattering for the penetrating neutrons and hence no reductions in the DFI signal. The magnets themselves completely attenuate the signal. This results in a noisy signal in the DFI without further information being able to be ascertained.

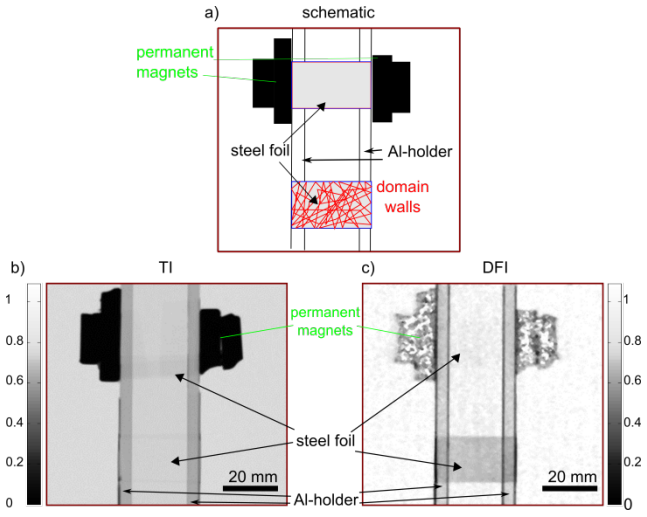

Figure 15: Magnetized and non-magnetized steel foil. In a) a schematic of the domain wall structure (red) in the magnetized and non-magnetized steel foil is shown. The upper foil is magnetized by neodymium magnets. In b) the TI of the two steel foils (20 µm thickness) is shown. One foil is mounted between neodymium magnets one is mounted without magnets. In the TI both foils are invisible. In the DFI of the two steel foils in c) the magnetized foil does not show a contribution while the non-magnetized does. The magnetic domain walls inside the lower foil refract the neutrons leading to a decreased DFI signal. The magnetized foil provides no inner domain walls resulting in no scattering and no degradation of the interference pattern. The aluminum holders as well as the neodymium magnets are visible in both images.

4 Preparation and tasks for the practical day

Preparation

1) How does a hysteresis loop look like for ferromagnetic samples, and what are the characteristic points of such a loop? What happens to magnetic domains and domain walls during a magnetization process? What is an initial magnetization curve, and how can one measure it?

2) Why are GRO laminations with a sharp Goss texture used in industrial transformer cores? How does a typical hysteresis loop like, and what should/could be improved?

3) What is a Moiré pattern and why they occur for an nGI setup and how we can benefit from them.

4) Describe with your own words and the white board why neutrons are refracted a magnetic domains. Calculate in which order the angle of deflection is.

5) In which direction (horizontal or vertical) the GRO lamination needs to be mounted to investigate the volume domain structure, and why?

6) Estimate the time for one DFI, when a typical exposure time for a raw image is 60s.

7) At which magnetic field values (region of the initial magnetization curve) should the DFIs be taken to visualize the changes of the volume magnetic domain structure?

Tasks

1) Installation of the nGI setup at the ICON beam line including the magnetization sample environment

2) Calibration of nGI setup such that no Moiré pattern remains

3) Determine the image resolution using the Gadolinium Siemens star test pattern

4) Get familiar to operate the camera software and the control software to run scripts for fully automated data acquisition

5) Take a set of open beam and dark current images

6) Take a DFI image to characterize the actual state of the sample

7) Demagnetize the sample to obtain the origin domain configuration

8) Take DFIs at different increasing field values to visualize the volume domain changes

9) Use the “nGI tool” to reconstruct the recorded raw images and process the corresponding DFI

5 Report

- The report you are writing should be in a style of a paper publication. Typically it contains an introduction and motivation, physical background of the scientific question, experimental setup and sample description, experimental results and a discussion/interpretation chapter.

- Try to write the report in a manner that you will be able to conduct this experiment again without help of the assistants. Think of a recipe in a cookbook! It hence should contain a logical chronology of activities you performed.

- The report should also contain the logbook and notes from the practical day.

6 References

Text books

E. Kneller, Ferromagnetismus (Springer, Berlin, 1962)

A. Hubert and R. Schaefer, Magnetic Domains (Springer, Berlin Heidelberg, 1998)

Papers

C. Grünzweig, F. Pfeiffer, O. Bunk, T. Donath, G. Kühne, G. Frei, M. Dierolf, and C. David
Design, fabrication, and characterization of diffraction gratings for neutron phase contrast imaging
Rev. Sci. Inst. **79**, 053703 (2008)

C. Grünzweig, C. David, O. Bunk, M. Dierolf, G. Frei, G. Kühne, J. Kohlbrecher, R. Schäfer, P. Lejcek, H. Rønnow, and F. Pfeiffer
Neutron decoherence imaging for visualizing bulk magnetic domain structures
Phys. Rev. Lett. **101**, 025504 (2008)

C. Grünzweig, C. David, O. Bunk, M. Dierolf, G. Frei, G. Kühne, R. Schäfer, S. Pofahl, H. Rønnow, and F. Pfeiffer
Bulk magnetic domain structures visualized by neutron dark-field imaging
Appl. Phys. Lett. **93**, 112504 (2008)

C. Grünzweig, C. David, O. Bunk, J. Kohlbrecher, E. Lehmann, Y. W. Lai, R. Schäfer, S. Roth, P. Lejcek, J. Kopecek, and F. Pfeiffer
Visualizing the propagation of volume magnetization in bulk ferromagnetic materials by neutron grating interferometry
J. Appl. Phys. **107**, 09D308 (2010)

I. Manke , N. Kardjilov , R. Schäfer , A. Hilger , M. Strobl , M. Dawson , C. Grünzweig , G. Behr, M. Hentschel , C. David , A. Kupsch , A. Lange and J. Banhart.
Three-dimensional imaging of magnetic domains
Nature Communications **1**, 125 (2010)

B. Betz, P. Rauscher, R. P. Harti, R. Schäfer, A. Irastorza-Landa, H. Van Swygenhoven, A. Kaestner, J. Hovind, E. Pomjakushina, E. Lehmann, and C. Grünzweig
Magnetization Response of the Bulk and Supplementary Magnetic Domain Structure in High-Permeability Steel Laminations Visualized In Situ by Neutron Dark-Field Imaging
Phys. Rev. Applied **6**, 024023 (2016)

B. Betz, P. Rauscher, R. P. Harti, R. Schäfer, H. Van Swygenhoven, A. Kaestner, J. Hovind, E. Lehmann, and C. Grünzweig
Frequency-Induced Bulk Magnetic Domain-Wall Freezing Visualized by Neutron Dark-Field Imaging
Phys. Rev. Applied **6**, 024024 (2016)

7 Practical information

Location:
This laboratory exercise is performed at the Swiss Neutron Spallation Source (SINQ) of the Paul Scherrer Institut (PSI). To find your way here please visit: http://www.psi.ch/how-to-find-us . You will be picked up at 9:00 at the entrance PSI-West. Use the bus stop “Villigen, PSI West”.

Time Schedule:
The LNS practical runs over one full day, starting at 09:00 and will finish at about 18:00. There will be plenty of time for breaks/lunch/coffee during the measurements.

Clothing/shoes:
This is a practical exercise and the SINQ facility at the ICON beam line. For the installation you will move around and handle experimental equipment that might not be particularly clean or “gentle”. Hence, we encourage the students to wear comfortable shoes.